Size-controlled engineering of cobalt metal catalysts through a coordination effect for oxygen electrocatalysis

Huihui Jin [a],[1], Ruohan Yu [b],[1], Chenxi Hu [b],[1], Pengxia Ji [b], Qianli Ma [b], Bingshuai Liu [b], Daping He [a],[c],[*], Shichun Mu [a],[b],[*]

[a] *Hubei Engineering Research Center of RF-Microwave Technology and Application, School of Science, Wuhan University of Technology, Wuhan 430070, China*
[b] *State Key Laboratory of Advanced Technology for Materials Synthesis and Processing, Wuhan University of Technology, Wuhan 430070, China*
[c] *State Key Laboratory of Silicate Materials for Architectures, Wuhan University of Technology, Wuhan 430070, China*

ABSTRACT

In the preparation process of carbon-based transition metal catalysts, the transition metal atoms usually seriously agglomerate, thus reducing the catalytic activity. To slow down the agglomeration of transition metal atoms during high-temperature treatments, herein, organics with coordination functions are proposed to regulate the typical metal-organic framework compound ZIF-67 with rich Co atoms. Electron microscopy structural characterization proves that ZIF-67 modified by coordinated organic compounds, including ascorbic acid (AA), citric acid (CA) and ethylenediaminetetraacetic acid disodium salt (EA), greatly improves the dispersibility of cobalt in the final product. All the adjusted ZIF-67 can derive cobalt-based bifunctional oxygen catalysts with higher activity. Among them, EA-MOF-Co shows the best ORR performance, with a half-wave potential comparable to commercial Pt/C in alkaline solutions and an obviously reduced oxygen evolution overpotential. This suggests that it is an effective method for use of coordination organics to tether metal ions and prevent their further agglomeration during carbonation.

1. Introduction

With the development of industrial civilization, the demand of energy for human beings is growing. Thus, it is crucial to develop new sustainable and green energy sources by some advanced energy conversion devices, such as fuel cells and metal-air batteries [1,2]. In recent years, due to high energy densities and no pollution, zinc-air batteries have become a hot research topic [3,4]. Nevertheless, the slow reaction kinetics of oxygen reduction (ORR) and oxygen evolution reaction (OER) greatly affect their applications [5,6]. Currently, noble metal catalysts such as Pt, Ir and Ru-based materials are the best catalyst to drive ORR and OER [7–9], but their scarce earth reserves, high prices, poor stability and resistance to poisoning seriously hinder the commercial application of zinc-air batteries. Definitely, it is imperative to develop non-noble metal catalysts with low cost, high electrochemical activity and stability.

Among the non-noble metal catalysts currently studied, carbon-based catalysts containing cobalt species generally exhibit bifunctional

catalytic activity (ORR and OER), and cobalt species typically including Co nanoparticles, Co-based oxides and Co-Nx [10–18]. There are many precursors for the preparation of cobalt-based carbon materials, in which 2-methylimidazole cobalt salt (ZIF-67) shows great potential for applications of ORR and OER catalysts with the advantages of abundant cobalt and N sources, large specific surface area, and rich pore structure [19–21]. However, it usually requires high-temperature pyrolysis for ZIF-67 to obtain the desired catalyst, in this case cobalt atoms spontaneously aggregate to form large-sized cobalt particles, resulting in reduction of electrochemically active surface area and active sites. Researchers usually introduce template or composite with other materials (such as graphene, carbon nanofibers, etc) to compensate for the deficiencies caused by the carbonization of ZIF-67 [22–26]. However, few have been investigated to control cobalt agglomeration, especially in the case of keeping the morphology unchanged.

Here, in order to reduce various adverse influencing factors caused by the carbonization of ZIF-67 itself, three different organic compounds with coordination functions (ascorbic acid, citric acid, and disodium

EDTA) were selected to tailor the division of Co in ZIF-67, ultimately improving the agglomeration of Co atoms in the carbonized products, thanks to their strong transition metal coordination capabilities. Morphological and structural characterization demonstrates that the agglomeration of Co is significantly weakened in the ZIF adjusted by the coordination organics during heat treatment. The electrochemical performance tests further show that the catalysts prepared with the coordination organic modification greatly enhance their oxygen electrocatalytic activity.

2. Experimental section

2.1. Synthesis of ZIF-67

Co(NO$_3$)$_2$.6 H$_2$O (0.581 g) was dissolved in 30 mL methanol solution, 2-methylimidazole (1.314 g) was dissolved in 30 mL methanol solution, and then mixed. After stirring in a 35 °C water bath for 4 h, the mixture was centrifuged, washed and dried in a vacuum oven.

2.2. Synthesis of AA-ZIF-67, CA-ZIF-67, EA-ZIF-67

vitamin C (AA, 0.045 g), citric acid (CA, 0.03 g) and disodium EDTA (EA, 0.055 g) were dissolved in 10 mL of deionized water, respectively. Co(NO$_3$)$_2$.6 H$_2$O (0.581 g) was dissolved in 30 mL methanol solution, and 2-methylimidazole (1.314 g) was dissolved in 30 mL methanol solution. The coordination organics were first mixed with the Co(NO$_3$)$_2$.6 H$_2$O solution, and then the mixture was poured into the 2-methylimidazole solution. After stirring in a 35 °C water bath for 4 h, the mixture was centrifuged, washed and dried in a vacuum oven. and named as AA-ZIF-67, CA-ZIF-67 and EA-ZIF-67, respectively.

2.3. Synthesis of MOF-Co, AA-MOF-Co, CA-MOF-Co and EA-MOF-Co

ZIF-67, AA-ZIF-67, CA-ZIF-67 and EA-ZIF-67 were placed in a tube furnace filled with argon atmosphere, heated up to 800 °C at a rate of 5 °C/min, then kept at 800 °C for 3 h, and finally naturally cooled to room temperature to obtain the catalysts. The products are named as MOF-Co, AA-MOF-Co, CA-MOF-Co and EA-MOF-Co according to the coordination organics used.
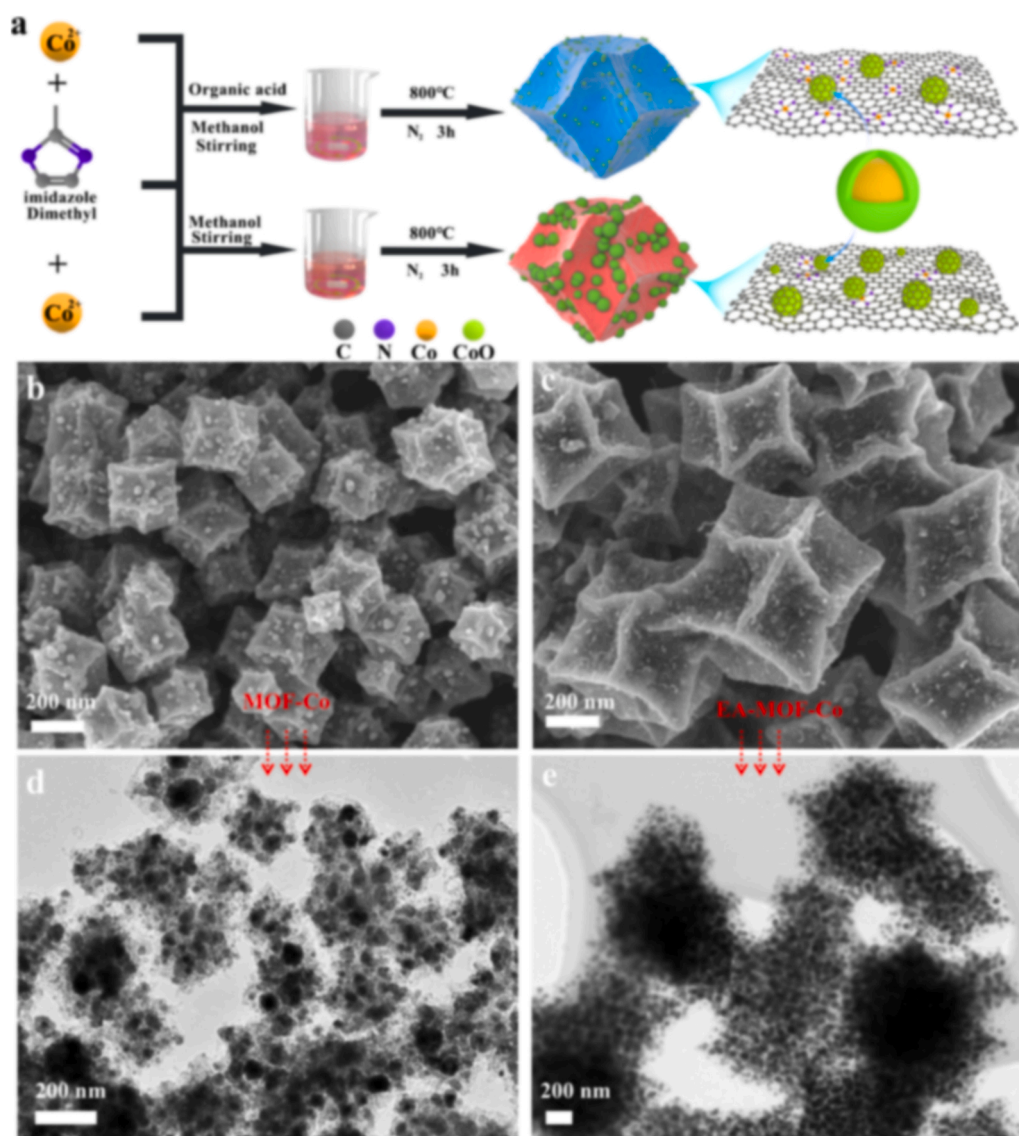

Fig. 1. (a) Synthetic strategy of MOF-derived electrocatalysts modulated by coordination organics; SEM images of (b) MOF-Co and (c) EA-MOF-Co; TEM images of (d) MOF-Co and (e) EA-MOF-Co.

3. Results and discussion

3.1. Morphology and structure characterization

The synthetic scheme of coordination organic regulation MOF is described in Fig. 1a. The coordination organics are dissolved simultaneously with cobalt nitrate, then mixed with 2-methylimidazole and subjected to a precipitation reaction for 4 h in a water bath environment at 35 °C. The coordination organics used in this experimental includes ascorbic acid, citric acid and ethylenediaminetetraacetic acid disodium salt (disodium EDTA). The corresponding prepared precursors are named AA-ZIF-67, CA-ZIF-67 and EA-ZIF-67, and the precursor prepared without the addition of coordinating organics is ZIF-67. The final catalyst is obtained by annealing the coordination organic regulation MOF precursor at 800 °C with N_2 flowing for 3 h. And the products obtained by calcination of ZIF-67, AA-ZIF-67, CA-ZIF-67 and EA-ZIF-67 are named MOF-Co, AA-MOF-Co, CA-MOF-Co and EA-MOF-Co, respectively.

XRD was first used to confirm the composition of all precursors. In Fig. S1a, the diffraction peaks of the MOFs treated with coordinated organics completely match those of pristine ZIF-67, which indicates that the crystal structure of ZIF-67 is not affected by the coordinated organics. In the FTIR spectra (Fig. S1b), compared to ZIF-67, AA-ZIF-67 and CA-ZIF-67 show enhanced C-O expansion vibration peaks around 1380 cm^{-1}, while EA-ZIF-67 presents enhanced C-O and C-N expansion vibration peaks around 1380 cm^{-1} and 1600 cm^{-1}, respectively, probably because more O and N are bonded to the metal. This also suggests that both ascorbic acid and citric acid provide O atoms to coordinate with cobalt, while disodium EDTA provides O and N atoms to coordinate with cobalt.

Since the coordination of organics and metals has been confirmed, the components of the final product are bound to be affected. In XRD patterns (Fig. S2a), the diffraction peaks in MOF-Co, AA-MOF-Co, CA-MOF-Co and EA-MOF-Co correspond to metal Co and CoO,

respectively. Comparing the peak intensities of the four samples, the peak intensities of metal Co and CoO decrease to different degrees after the addition of coordination organics, manifesting that the content or size of the cobalt particles in the samples decreased [27,28]. It also implies that the agglomeration of cobalt ions on the catalyst surface is alleviated after the treatment with coordination organics. Followed by Raman spectra, the ID/IG value of MOF-Co can be calculated as 1.01, which is smaller than that of AA-MOF-Co (1.02), CA-MOF-Co (1.03) and EA-MOF-Co (1.14) (where D denotes defects and G denotes graphitization) (Fig. S2b) [29,30], suggesting that the use of coordination organics may cause more defects in the products.

SEM images show that all the as-prepared samples exhibit a rhombic dodecahedron morphology (Figs. 1b, c, S3), indicating that the coordination organics would not affect the morphology of the catalyst. Apparently, there are many large particles on the surface of MOF-Co, while the surfaces of AA-MOF-Co, CA-MOF-Co and EA-MOF-Co are relatively smooth and the particle sizes are significantly reduced. Further comparison of the four products by TEM images confirm that the particles in MOF-Co are very heterogeneous in size, but all the products obtained by the modulation of coordinated organics have more homogeneous or smaller size particles (Figs. 1d, e, S4). Especially, the particles in EA-MOF-Co are well distributed and uniform in size.

Fig. 2a shows the particle size of about 50 nm in EA-MOF-Co, the particle in EA-MOF-Co is core-shell structure, where the diameter of the core is about 15–20 nm and the shell is about 10–15 nm (Fig. 2b). From the HRTEM image, two kinds of lattice stripes exist on the particles. Then according to the XRD results, the lattice spacing of approximately 0.2 nm in the core region was preliminary determined to represent the (111) crystal plane of metallic Co, and the lattice spacing of approximately 0.213 nm in the shell region was initially determined to represent the (200) crystal plane of CoO (Fig. 2c). Strikingly, many monodisperse Co atoms are present in the surface of carbon matrix (red circles in Fig. 2d). Through EELS analysis, these single atoms can be judged as Co-N coordination (Fig. 2e). The HAADF-STEM EDS mapping
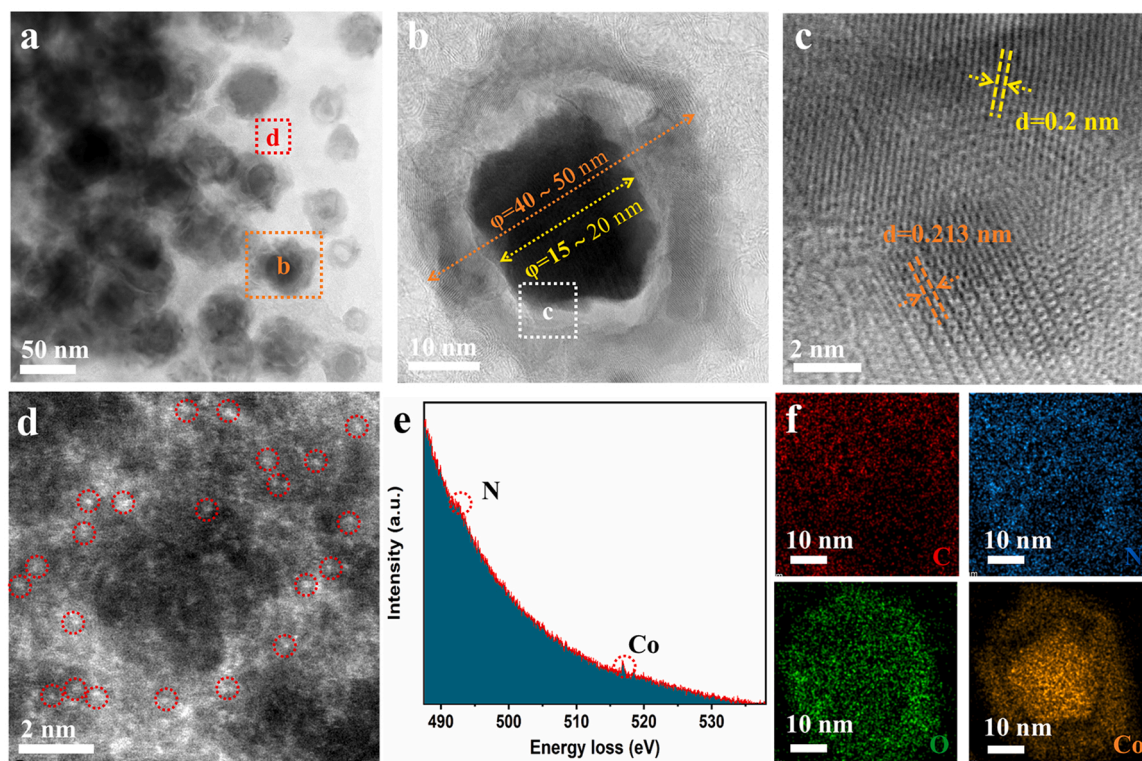

Fig. 2. Morphology and structure of EA-MOF-Co. (a) and (b) TEM images, (c) HRTEM image, (d) aberration-corrected HAADF-STEM image, (e) monodisperse Co atoms structure analyzed by EELS, (f) HAADF-STEM EDS mapping.

of the particle shows that C and N are uniformly dispersed (Fig. 2f), while the core and shell regions are mainly gathered with the Co atom and the Co and O atoms, respectively. Therefore, the aforementioned test results collectively demonstrate that this particle in EA-MOF-Co is structured with metallic cobalt as the core and cobalt oxide as the shell.

To further analyze the effect of the use of coordination organics on the fine chemical structure of the samples, XPS test was performed. C1s spectrum can be fitted as five peaks, namely C-sp2 (284.5 eV), C-sp3 (285 eV), C-N (285.5 eV), C-O (286.5 eV) and C=O (288.2 eV) (Fig. S5) [31,32]. The C-N bond content is significantly increased in the samples prepared with coordination organics, which favors the electrochemical performance.[33,34] The N1s high-resolution XPS spectrum is usually divided into three peaks located at 398.9 eV, 400.1 eV and 401.2 eV, representing pyridinic-N (pyri-N), pyrrolic-N (pyrr-N) and graphitic-N (grap-N), respectively (Fig. S6) [35,36]. Among them, pyri-N is the active site for the oxygen reduction reaction and grap-N has the ability to stabilize the carbon materials [37,38]. Moreover, pyri-N and grap-N are also the most active nitrogen species in the oxygen evolution reaction [39,40]. Compared with MOF-Co, the content of pyri-N and grap-N is increased for catalysts prepared with the coordination organics, resulting in more active sites and increased stability for ORR and OER. The Co2p XPS pattern includes two core energy regions: Co 2p1/2 and Co 2p3/2 (Fig. S7) [41,42]. By peak area comparison, the content of Co^0 for AA-MOF-Co, CA-MOF-Co and EA-MOF-Co is significantly decreased, in accordance with the XRD test results. Meanwhile, the content of Co^{2+} is obviously increased, which may also indicate the increase of Co^{2+}-N. All the above results demonstrate that the addition of coordination organics slows down the agglomeration of Co, reduces the size of Co particles, and promotes the generation of Co-Nx active sites, all of which are very favorable for the electrocatalytic reaction.

3.2. Oxygen reduction reaction performance

The ORR electrocatalytic performance of these samples was first measured in 0.1 M KOH. LSV curves display that the half-wave potential ($E_{1/2}$) of AA-MOF-Co, CA-MOF-Co and EA-MOF-Co are all increased compared to MOF-Co (Fig. 3a), with the highest $E_{1/2}$ of 0.842 V for EA-MOF-Co, which is comparable to 20% Pt/C. The reduced Tafel slopes of

the samples prepared with the coordination organics also evidence their faster electrochemical reaction rate (Fig. 3b). Subsequently, EA-MOF-Co was subjected to the LSV tests at six different rotational speeds, and then the K-L plot was obtained on the basis of the Koutecky-Levich (K-L) equation. The five parallel curves signify that the ORR process of EA-MOF-Co is consistent with the first-order kinetics (Fig. 3c). The electron transfer number was calculated to be 3.99, uncovering that EA-MOF-Co has the ability to convert oxygen directly into H_2O, reducing the generation of by-products such as H_2O_2, beneficial to the stability of the catalyst.

Fig. 3d shows the LSV curves before and after 10,000 CV cycles, and the ORR activity of EA-MOF-Co maintains excellent stability. Additionally, EA-MOF-Co can maintain a 96.2% current density after 7 h of chronoamperometry test, while 20% Pt/C drops to 81.3% in less than 3 h of test (Fig. 3e). TEM images show that the morphology and size of the particle in EA-MOF-Co remain unchanged after the ORR stability testing (Fig. S8). In addition, the XPS binding energy positions of Co2p and O1s of EA-MOF-Co are consistent before and after the ORR stability test (Fig. S9), indicating that the components of EA-MOF-Co are almost unchanged. Then, the methanol resistance of the sample was tested with chronoamperometry. After pouring methanol into the electrolyte, EA-MOF-Co gradually stabilizes after a short fluctuation and the current density almost has no change, while the current density of 20% Pt/C is decreased sharply (Fig. 3f). The above test results strongly corroborate that EA-MOF-Co has excellent stability.

Since EA-MOF-Co donates the best half-wave potential in alkaline electrolyte, its ORR activity in acidic electrolyte (0.5 M H_2SO_4) was continued to be examined. Fig. S10a shows the LSV curves of EA-MOF-Co, MOF-Co and 20% Pt/C in 0.5 M H_2SO_4. Although the half-wave potential of EA-MOF-Co is lower than 20% Pt/C, there is a significant increase relative to MOF-Co, which also reflects the positive modulation of ZIF-67 by disodium EDTA. The electron transfer number obtained from K-L equation confirms the excellent ability of EA-MOF-Co to reduce oxygen under acidic conditions (Fig. S10b). Undoubtedly, EA-MOF-Co still maintains its better stability and resistance to methanol in 0.5 M H_2SO_4 (Fig. S10c, d).
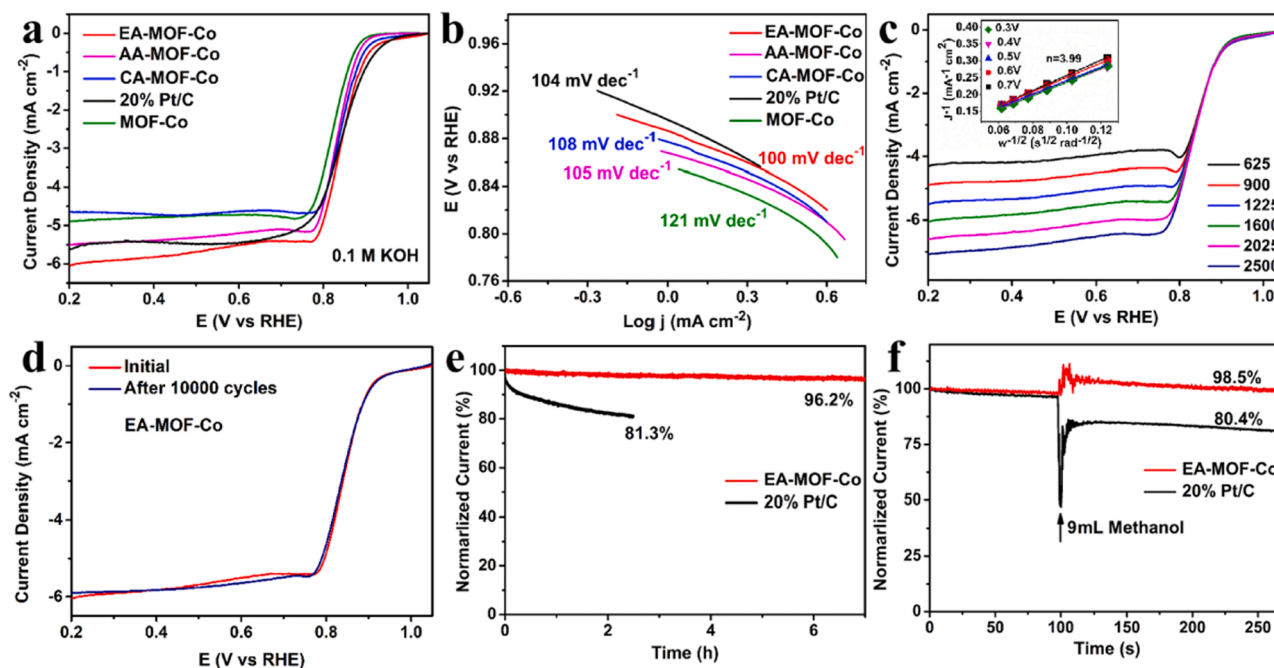

Fig. 3. ORR performance in alkaline electrolytes. (a) LSV curves, (b) Tafel plots, (c) LSV curves of EA-MOF-Co at different rotation rates (inset: corresponding Koutecky-Levich plots), (d) LSV curves of EA-MOF-Co before and after 10,000 CV cycles, (e) i-t curves and (f) methanol resistance test.

3.3. Oxygen evolution reaction performance

Immediately, the catalysts prepared with the coordination organic modification were again compared with MOF-Co and RuO$_2$ in a 1 M KOH electrolyte for OER activity. Their OER activities were first recorded by LSV test (Fig. 4a). The overpotentials of EA-MOF-Co, AA-MOF-Co and CA-MOF-Co are 389 mV, 402 mV and 405 mV at 10 mA cm^{-2}, respectively (Fig. 4b). Although slightly larger than RuO$_2$ (324 mV), they are significantly lower than MOF-Co (443 mV), suggesting that the OER activity is substantially improved by adding the coordination organic. The Tafel slope also reveals that the catalysts prepared with coordination organics have faster reaction kinetics than MOF-Co (Fig. 4c). Electrochemical impedance (EIS) tests were then carried out on the samples to characterize the charge transfer rates during the OER process. The smaller semicircle diameter of EA-MOF-Co AA-MOf-Co and CA-MOF-Co reflects their lower resistance and faster charge transfer rate (Fig. 4d), which is favorable to their OER activity.

Afterward, the CV curves outside the faraday region at five sweep speeds were tested to calculate the electric double layer capacitance (Cdl) (Fig. S11). The Cdl value of EA-MOF-Co, AA-MOF-Co and CA-MOF-Co is 52.1 mF cm^{-2}, 49.7 mF cm^{-2} and 43.6 mF cm^{-2}, respectively, but that of MOF-Co is only 15.5 mF cm^{-2} (Fig. 4e), meaning that the catalysts prepared with coordination organics, especially EA-MOF-Co, have larger electrochemically active surface area. Moreover, the specific surface area of EA-MOF-Co, AA-MOF-Co , CA-MOF-Co and MOF-Co was analyzed by N$_2$ adsorption/desorption isothermal measurements, their specific surface area is 347.57 m^2 g^{-1}, 298.1 m^2 g^{-1}, 289.16 m^2 g^{-1} and 266.31 m^2 g^{-1}, respectively (Fig. S12, Table S1), consistent with the Cdl results. In addition, the N$_2$ adsorption/desorption isothermal results show that EA-MOF-Co, AA-MOF-Co , CA-MOF-Co possess a larger pore capacity than MOF-Co. Larger specific surface area is beneficial to expose active center [43,44] and larger pore capacity is convenient to accommodate more electrolyte [45,46], thus leading to improved electrochemical performance.

Furthermore, the stability of the best catslyst EA-MOF-Co was tested by CV accelerated cycling and chronoamperometry. With 10,000 CV cycles acceleration testing, the OER activity of EA-MOF-Co has slightly increased, which may be due to the activation of surface components and increase of electrode wettability by CV cycling [47,48] (Fig. S13). In addition, the chronoamperometry result also testifies that EA-MOF-Co has excellent stability to OER, and the current density of EA-MOF-Co decreases by only 8.2% within 9 h (Fig. 4f). Fig. S14 shows the morphology of EA-MOF-Co after OER stability test, the particles in EA-MOF-Co still maintain the core-shell structure after the OER stability test, implying that the particle structure has excellent stability. XPS spectra of Co2p show that Co shifts towards to lower binding energy after OER stability test (Fig. S15a), attributive to the formation of Co^{3+}. Then, through the change of O1s binding energy (Fig. S15b), it can be determined that CoOOH was generated on EA-MOF-Co after the OER stability test, as a result of the oxidation of cobalt species on the surface of EA-MOF-Co by electrochemical activation and also the active material for OER.

3.4. Zinc-air battery application

Due to the good ORR and OER performance of EA-MOF-Co, a practical liquid rechargeable zinc-air cell was constructed (Fig. 5a), with a polished zinc foil as the anode, a carbon paper coated with catalyst as the cathode, and 6.0 M potassium hydroxide solution dissolved with 0.2 M zinc acetate as the electrolyte. The open-circuit voltage of the EA-MOF-Co-based zinc-air battery is 1.485 V, but it is only 1.445 V for 20% Pt/C+RuO$_2$ (Fig. S16). Fig. 5b shows a peak power density of 111 mW cm^{-2} for the EA-MOF-Co-based zinc-air battery, higher than that of 20% Pt/C+RuO$_2$ (92 mW cm^{-2}). Moreover, it discharges a plateau of 1.315 V at the current density of 5 mA cm^{-2}, better than 20% Pt/C+RuO$_2$ (1.289 V), and remains stable throughout the 80,000 s test (Fig. 5c), exhibiting a good discharge stability. Besides, based on the discharge of the zinc-air battery with EA-MOF-Co at a current density of 20 mA cm^{-2} (the discharge duration was 28.56 h, average discharge voltage was 1.28 V) and the mass of the zinc sheet consumed (0.8 g), the specific energy and the energy density of the battery were calculated to be 714 mAh/g$_{Zn}$ and 914 Wh/kg$_{Zn}$, respectively, which is comparable to the performance of most zinc-air batteries from the literature (Fig. S17, Table S2). Moreover, the stable galvanostatic discharge and charge
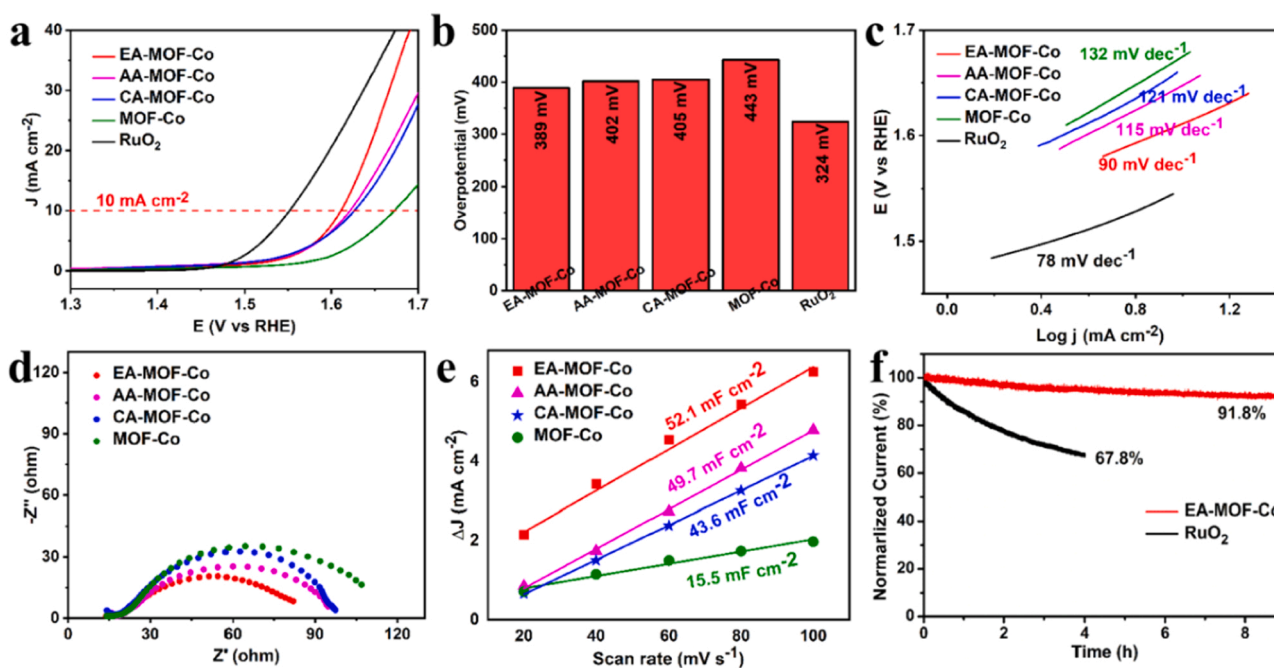

Fig. 4. OER performance evaluation. (a) LSV curves, (b) overpotentials summary at 10 mA cm^{-2}, (c) Tafel plots, (d) Nyquist plots for MOF-Co, CA-MOF-Co, AA-MOF-Co and EA-MOF-Co obtained at 1.65 V, (e) the current density variation at 0.15 V versus Hg/HgO plotted against with the scan rates, (f) i-t curves of EA-MOF-Co and RuO$_2$.
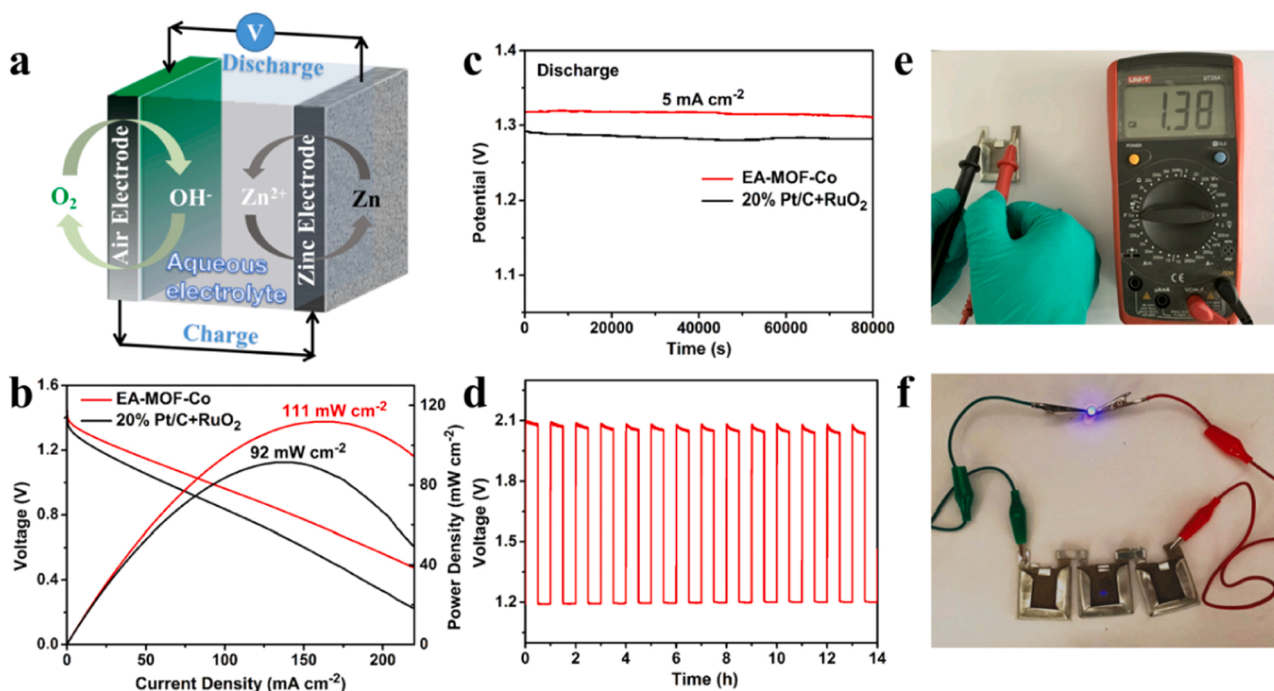
Fig. 5. Zinc-air battery performance evaluation. (a) Assembled zinc air battery, (b) power density curves, (c) discharge curves under 5 mA cm^{-2}, (d) galvanostatic charge-discharge cycling of EA-MOF-Co based zinc-air battery, (e) picture of open circuit voltage of solid zinc-air battery and (f) a lighted LED (~3.4 V).

cycling for 14 h proves its excellent charge/discharge stability (Fig. 5d). Furthermore, EA-MOF-Co was assembled in the all-solid-state zinc-air battery as the air cathode. The all-solid-state zinc-air battery outputs a high open-circuit voltage of 1.38 V and can light a small bulb with a voltage of about 3.4 V by connecting only three of these all-solid-state zinc-air batteries in series (Fig. 5e, f). The above performance of EA-MOF-Co in zinc-air batteries affirms its excellent practical catalytic performance.

4. Conclusion

In summary, we have successfully adjusted the MOF using coordination organics to prepare highly efficient cobalt-based oxygen reduction/oxygen evolution bifunctional catalysts. The introduction of coordination organics had no destructive effect on the morphology of the catalyst, but it obviously reduced the size of cobalt particles in the catalyst and enriches the content of Co-N_x sites. As expected, the ORR and OER activities of the catalysts prepared with coordination organics are both improved. This study has implications for the size-controlled engineering of metal particles and the design of efficient bifunctional electrocatalysts.

CRediT authorship contribution statement

Huihui Jin: Conceptualization, Methodology, Writing − original draft preparation. **Ruohan Yu, Chenxi Hu:** Methodology, Analysis. **Pengxia Ji, Qianli Ma, Bingshuai Liu:** Discussion. **Shichun Mu, Daping He:** Writing − review & editing, Validation.

Declaration of Competing Interest

The authors declare that they have no known competing financial interests or personal relationships that could have appeared to influence the work reported in this paper.

Appendix A. Supporting information

Supplementary data associated with this article can be found in the online version at doi:10.1016/j.apcatb.2022.121766.

References

[1] Y. Wang, D. Diaz, K. Chen, Z. Wang, X. Adroher, Materials, technological status, and fundamentals of PEM fuel cells-a review, Mater. Today 32 (2020) 178–203, https://doi.org/10.1016/j.mattod.2019.06.005.

[2] S. Shi, X. Wen, Q. Sang, S. Yin, K. Wang, J. Zhang, M. Hu, H. Yin, J. He, Y. Ding, Ultrathin nanoporous metal electrodes facilitate high proton conduction for low-Pt PEMFCs, Nano Res. 14 (2021) 2681–2688, https://doi.org/10.1007/s12274-020-3272-0.

[3] Y. Deng, Y. Jiang, R. Liang, S. Zhang, D. Luo, Y. Hu, X. Wang, J. Li, A. Yu, Z. Chen, Dynamic electrocatalyst with current-driven oxyhydroxide shell for rechargeable zinc-air battery, Nat. Commun. 11 (2020) 1952, https://doi.org/10.1038/s41467-020-15853-1.

[4] Z. Pei, Z. Yuan, C. Wang, S. Zhao, J. Fei, L. Wei, J. Chen, C. Wang, R. Qi, Z. Liu, A. Chen, A flexible rechargeable zinc-air battery with excellent low-temperature adaptability, Angew. Chem. Int. Ed. 59 (2020) 4793–4799, https://doi.org/10.1002/anie.201915836.

[5] Z. Sun, Y. Wang, L. Zhang, H. Wu, Y. Jin, Y. Li, Y. Shi, T. Zhu, H. Mao, J. Liu, C. Xiao, S. Ding, Simultaneously realizing rapid electron transfer and mass transport in jellyfish-like mott-schottky nanoreactors for oxygen reduction reaction, Adv. Funct. Mater. 30 (2020) 1910482, https://doi.org/10.1002/adfm.201910482.

[6] L. Tian, X. Zhai, X. Wang, J. Li, Z. Li, Advances in manganese-based oxides for oxygen evolution reaction, J. Mater. Chem. A 8 (2020) 14400–14414, https://doi.org/10.1039/d0ta05116k.

[7] W. Li, Z. Hu, Z. Zhang, P. Wei, J. Zhang, Z. Pu, J. Zhu, D. He, S. Mu, G. Tendeloo, Nano-single crystal coalesced PtCu nanospheres as robust bifunctional catalyst for hydrogen evolution and oxygen reduction reactions, J. Catal. 375 (2019) 164–170, https://doi.org/10.1016/j.jcat.2019.05.031.

[8] B. Hu, X. Deng, L. Zhou, J. Dai, G. Yang, W. Tan, W. Zhou, Z. Shao, Facile synthesis of synergistic Pt/(Co-N)@C composites as alternative oxygen-reduction electrode

of PEMFCs with attractive activity and durability, Compos. Part B: Eng. 193 (2020) 108012, https://doi.org/10.1016/j.compositesb.2020.108012.

[9] M. Hubert, A. Patel, A. Gallo, Y. Liu, E. Valle, M. Ben-Naim, J. Sanchez, D. Sokaras, R. Sinclair, J. Nørskov, L. King, M. Bajdich, T. Jaramillo, Acidic oxygen evolution reaction activity-stability relationships in Ru-based pyrochlores, ACS Catal. 10 (2020) 12182–12196, https://doi.org/10.1021/acscatal.0c02252.

[10] M. Wu, G. Zhang, H. Tong, X. Liu, L. Du, N. Chen, J. Wang, T. Sun, T. Regierd, S. Sun, Cobalt (II) oxide nanosheets with rich oxygen vacancies as highly efficient bifunctional catalysts for ultra-stable rechargeable Zn-air flow battery, Nano Energy 79 (2021), 105409, https://doi.org/10.1016/j.nanoen.2020.105409.

[11] B.Y. Guan, L. Yu, X.W. Lou, Formation of single-holed Cobalt/N-doped carbon hollow particles with enhanced electrocatalytic activity toward oxygen reduction reaction in alkaline media, Adv. Sci. 4 (2017) 1700247, https://doi.org/10.1002/advs.201700247.

[12] J. Zhou, L. Zhang, Y.C. Huang, C. Dong, H. Lin, C. Chen, L. Tjeng, Z. Hu, Voltage- and time-dependent valence state transition in cobalt oxide catalysts during the oxygen evolution reaction, Nat. Commun. 11 (2020) 1984, https://doi.org/10.1038/s41467-020-15925-2.

[13] Y. Tian, L. Xu, M. Li, D. Yuan, X. Liu, J. Qian, Y. Dou, J. Qiu, S. Zhang, Interface engineering of CoS/CoO@N-doped graphene nanocomposite for high-performance rechargeable Zn-air batteries, Nano-Micro Lett. 13 (2021) 97, https://doi.org/10.1007/s40820-020-00526-x.

[14] X. Liu, L. Zhang, H. Xu, Q. Huang, Y. Wang, C. Hou, Y. Hou, J. Wang, F. Dang, J. Zhang, Tunable cationic vacancies of cobalt oxides for efficient electrocatalysis in Li-O₂ batteries, Adv. Energy Mater. 10 (2020) 2001415, https://doi.org/10.1002/aenm.202001415.

[15] H. Pan, X. Huang, Z. Lu, Z. Zhang, B. An, D. Wu, T. Wang, X. Chen, F. Cheng, Dual oxidation and sulfurization enabling hybrid Co/Co₃O₄@CoS in S/ N-doped carbon matrix for bifunctional oxygen electrocatalysis and rechargeable Zn-air batteries, Chem. Eng. J. 419 (2021), 129619, https://doi.org/10.1016/j.cej.2021.129619.

[16] X.F. Lu, Y. Chen, S.B. Wang, S.Y. Gao, X.W. Lou, Interfacing manganese oxide and cobalt in porous graphitic carbon polyhedrons boosts oxygen electrocatalysis for Zn-air batteries, Adv. Mater. 31 (2019) 1902339, https://doi.org/10.1002/adma.201902339.

[17] S.S. Li, X.G. Hao, A. Abudula, G.Q. Guan, Nanostructured co-based bifunctional electrocatalysts for energy conversion and storage: current status and perspectives, J. Mater. Chem. A 7 (2019) 18674, https://doi.org/10.1039/C9TA04949E.

[18] X.F. Lu, S.L. Zhang, E.B. Shangguan, P. Zhang, S.Y. Gao, X.W. Lou, Nitrogen-doped cobalt pyrite yolk-shell hollow spheres for long-life rechargeable Zn-air batteries, Adv. Sci. 7 (2020) 2001178, https://doi.org/10.1002/advs.202001178.

[19] Y. Guan, Y.L. Li, S. Luo, X.Z. Ren, L.B. Deng, L.N. Sun, H.W. Mi, P.X. Zhang, J. H. Liu, Rational design of positive-hexagon-shaped two-dimensional ZIF-derived materials as improved bifunctional oxygen electrocatalysts for use as long-lasting rechargeable Zn-air batteries, Appl. B: Environ. 256 (2019), 117871, https://doi.org/10.1016/j.apcatb.2019.117871.

[20] M.H. Zhang, E.H. Zhang, C.Y. Hu, Y. Zhao, H.M. Zhang, Y.J. Zhang, M.W. Ji, J. L. Yu, G.T. Cong, H.C. Liu, J.T. Zhang, C.Z. Zhu, J. Xu, Controlled synthesis of Co@ N-doped carbon by pyrolysis of ZIF with 2-aminobenzimidazole ligand for enhancing oxygen reduction reaction and the application in Zn-air battery, ACS Appl. Mater. Interfaces 12 (2020) 11693, https://doi.org/10.1021/acsami.9b22476.

[21] X.F. Lu, Y.J. Fang, D.Y. Luan, X.W. Lou, Metal-organic frameworks derived functional materials for electrochemical energy storage and conversion: a mini review, Nano Lett. 21 (2021) 1555, https://doi.org/10.1021/acs.nanolett.0c04898.

[22] Y. Zhang, P. Wang, J. Yang, S. Lu, K. Li, G. Liu, Y. Duan, J. Qiu, Decorating ZIF-67-derived cobalt-nitrogen doped carbonnanocapsules on 3D carbon frameworks for efficient oxygen reduction and oxygen evolution, Carbon 177 (2021) 344–356, https://doi.org/10.1016/j.carbon.2021.02.052.

[23] X. Sun, S. Sun, S. Gu, Z. Liang, J. Zhang, Y. Yang, Z. Deng, P. Wei, J. Peng, Y. Xu, C. Fang, Q. Li, J. Han, Z. Jiang, Y. Huang, High-performance single atom bifunctional oxygen catalysts derived from ZIF-67 superstructures, Nano Energy 61 (2019) 245–250, https://doi.org/10.1016/j.nanoen.2019.04.076.

[24] W. Zhang, X. Yao, S. Zhou, X. Li, L. Li, Z. Yu, L. Gu, ZIF-8/ZIF-67-derived Co-Nx-embedded 1D porous carbon nanofibers with graphitic carbon-encased Co nanoparticles as an efficient bifunctional electrocatalyst, Small 14 (2018) 1800423, https://doi.org/10.1002/smll.2018.

[25] W. Peng, X. Yang, L. Mao, J. Jin, S. Yang, J. Zhang, G. Li, ZIF-67-derived Co nanoparticles anchored in N doped hollow carbon nanofibers as bifunctional oxygen electrocatalysts, Chem. Eng. J. 407 (2021) 127157, https://doi.org/10.1016/j.cej.2020.127157.

[26] Z. Zhang, Y. Tan, T. Zeng, L. Yu, R. Chen, N. Cheng, S. Mu, X. Sun, Tuning the dual-active sites of ZIF-67 derived porous nanomaterials for boosting oxygen catalysis and rechargeable Zn-air batteries, Nano Res. 14 (2021) 2353–2362, https://doi.org/10.1007/s12274-020-3234-6.

[27] X. Shu, Q. Yang, F. Yao, Y. Zhong, W. Ren, F. Chen, J. Sun, Y. Ma, Z. Fu, D. Wang, X. Li, Electrocatalytic hydrodechlorination of 4-chlorophenol on Pd supported multi-walled carbon nanotubes particle electrodes, Chem. Eng. J. 358 (2019) 903–911, https://doi.org/10.1016/j.cej.2018.10.095.

[28] V. Nguyen, N. Nguyen, Y. Ali, Q. Tran, H. Choi, Graphene dot armored ptmo nanosponge as a highly efficient and stable electrocatalyst for hydrogen evolution reactions in both acidic and alkaline media, Carbon 146 (2019) 116–124, https://doi.org/10.1016/j.carbon.2019.01.087.

[29] L. Zong, K. Fan, W. Wu, L. Cui, L. Zhang, B. Johannessen, D. Qi, H. Yin, Y. Wang, P. Liu, L. Wang, H. Zhao, Anchoring single copper atoms to microporous carbon

[30] spheres as high-performance electrocatalyst for oxygen reduction reaction, Adv. Funct. Mater. 31 (2021) 2104864, https://doi.org/10.1002/adfm.20210486.

[30] S. Riyajuddin, K. Azmi, M. Pahuja, S. Kumar, T. Maruyama, C. Bera, K. Ghosh, Super-hydrophilic hierarchical Ni-foam-graphene-carbon nanotubes-Ni₂P-CuP₂ nano-architecture as efficient electrocatalyst for overall water splitting, ACS Nano 15 (2021) 5586–5599, https://doi.org/10.1021/acsnano.1c00647.

[31] J. Liu, C. Wang, H. Sun, H. Wang, F. Rong, L. He, Y. Lou, S. Zhang, Z. Zhang, M. Du, CoOx/CoNy nanoparticles encapsulated carbon-nitride nanosheets as an efficiently trifunctional electrocatalyst for overall water splitting and Zn-air battery, Appl. Catal. B: Environ. 279 (2020), 119407, https://doi.org/10.1016/j.apcatb.2020.119407.

[32] G. Daniel, Y. Zhang, S. Lanzalaco, F. Brombin, T. Kosmala, G. Granozzi, A. Wang, E. Brillas, I. Sirés, C. Durante, Chitosan-derived nitrogen-doped carbon electrocatalyst for a sustainable upgrade of oxygen reduction to hydrogen peroxide in UV-assisted electro-fenton water treatment, ACS Sustain. Chem. Eng. 8 (2020) 14425–14440, https://doi.org/10.1021/acssuschemeng.0c04294.

[33] Z. Lu, J. Chen, W. Wang, W. Li, M. Sun, Y. Wang, X. Wang, J. Ye, H. Rao, Electrocatalytic, kinetic, and mechanism insights into the oxygen-reduction catalyzed based on the biomass-derived FeOx@N-doped porous carbon composites, Small 17 (2021) 2007326, https://doi.org/10.1002/smll.202007326.

[34] C. Zhao, S. Zhang, M. Han, X. Zhang, Y. Liu, W. Li, C. Chen, G. Wang, H.M. Zhang, H.J. Zhang, Ambient electrosynthesis of ammonia on a biomass-derived nitrogen-doped porous carbon electrocatalyst: contribution of pyridinic nitrogen, ACS Energy Lett. 4 (2019) 377–383, https://doi.org/10.1021/acsenergylett.8b02138.

[35] W. Ye, Y. Yang, M. Arif, S. Yang, X. Fang, M. Mushtaq, X. Chen, D. Yan. Fe, Mo-N/C hollow porous nitrogen-doped carbon nanorods as an effective electrocatalyst for N₂ reduction reaction, ACS Sustain. Chem. Eng. 8 (2020) 15946–15952, https://doi.org/10.1021/acssuschemeng.0c05523.

[36] S. Li, J. Shu, S. Ma, H. Yang, J. Jin, X. Zhang, R. Jin, Engineering three-dimensional nitrogen-doped carbon black embedding nitrogen-doped graphene anchoring ultrafine surface-clean pd nanoparticles as efficient ethanol oxidation electrocatalyst, Appl. Catal. B: Environ. 280 (2021), 119464, https://doi.org/10.1016/j.apcatb.2020.119464.

[37] Q. Wang, Y. Ji, Y. Lei, Y. Wang, Y. Li, S. Wang, Pyridinic-N-dominated doped defective graphene as a superior oxygen electrocatalyst for ultrahigh-energy-density Zn-air batteries, ACS Energy Lett. 3 (2018) 1183–1191, https://doi.org/10.1021/acsenergylett.8b00303.

[38] S. Wang, H. Wang, C. Huang, P. Ye, X. Luo, J. Ning, Y. Zhong, Y. Hu, Trifunctional electrocatalyst of N-doped graphitic carbon nanosheets encapsulated with CoFe alloy nanocrystals: the key roles of bimetal components and high-content graphitic-N, Appl. Catal. B: Environ. 298 (2021), 120512, https://doi.org/10.1016/j.apcatb.2021.120512.

[39] S. Li, Y. Gao, N. Li, L. Ge, X. Bu, P. Feng, Transition metal-based bimetallic MOFs and MOF-derived catalysts for electrochemical oxygen evolution reaction, Energy Environ. Sci. 14 (2021) 1897–1927, https://doi.org/10.1039/d0ee03697h.

[40] L. Zhong, C. Jiang, M. Zheng, X. Peng, T. Liu, S. Xi, X. Chi, Q. Zhang, L. Gu, S. Zhang, G. Shi, L. Zhang, K. Wu, Z. Chen, T. Li, M. Dahbi, J. Alami, K. Amine, J. Lu, Wood carbon based single-atom catalyst for rechargeable Zn-air batteries, ACS Energy Lett. 6 (2021) 3624–3633, https://doi.org/10.1021/acsenergylett.1c01678.

[41] M. Tan, Y. Xiao, W. Xi, X. Lin, B. Gao, Y. Chen, Y. Zheng, B. Lin, Cobalt-nanoparticle impregnated nitrogen-doped porous carbon derived from schiff-base polymer as excellent bifunctional oxygen electrocatalysts for rechargeable zinc-air batteries, J. Power Sources 490 (2021), 229570, https://doi.org/10.1016/j.jpowsour.2021.229570.

[42] X. Shi, Z. Xu, C. Han, R. Shi, X. Wu, B. Lu, J. Zhou, S. Liang, Highly dispersed cobalt nanoparticles embedded in nitrogen-doped graphitized carbon for fast and durable potassium storage, Nano-Micro Lett. 13 (2021) 21, https://doi.org/10.1007/s40820-020-00534-x.

[43] Z. Ye, Y. Jiang, L. Li, R. Chen, Self-Assembly of 0D–2D Heterostructure Electrocatalyst from MOF and MXene for Boosted Lithium Polysulfide Conversion Reaction, Adv. Mater. 33 (2021) 2101204, https://doi.org/10.1002/adma.202101204.

[44] N. Mubarak, M. Ihsan-Ul-Haq, H. Huang, J. Cui, S. Yao, A. Susca, J. Wu, M. Wang, X. Zhang, B. Huang, J. Kim, Metal-organic framework-induced mesoporous carbon nanofibers as an ultrastable Na metal anode host, J. Mater. Chem. A 8 (2020) 10269–10282, https://doi.org/10.1039/d0ta00359j.

[45] M. Tavakkoli, E. Flahaut, P. Peljo, J. Sainio, F. Davodi, E. Lobiak, K. Mustonen, E. Kauppinen, Mesoporous single-atom-doped graphene-carbon nanotube hybrid: synthesis and tunable electrocatalytic activity for oxygen evolution and reduction reactions, ACS Catal. 10 (2020) 4647–4658, https://doi.org/10.1021/acscatal.0c00352.

[46] M. Tian, Y. Zhu, Y. Chen, X. Liu, Y. Yang, S. Gao, Template-assisted self-activation of mesoporous carbon with active nitrogen/oxygen configurations for sustainable triboelectric nanogenerator powered electro-fenton degradation, Nano Energy 83 (2021), 105825, https://doi.org/10.1016/j.nanoen.2021.105825.

[47] S. Gupta, S. Zhao, X.X. Wang, S. Hwang, S. Karakalos, S. Devaguptapu, S. Mukherjee, D. Su, H. Xu, G. Wu, Quaternary FeCoNiMn-based nanocarbon electrocatalysts for bifunctional oxygen reduction and evolution: promotional role of Mn doping in stabilizing carbon, ACS Catal. 7 (2017) 8386–8393, https://doi.org/10.1021/acscatal.7b02949.

[48] Y.T. He, X.X. Yang, Y.S. Li, L.T. Liu, S.W. Guo, C.Y. Shu, F. Liu, Y.N. Liu, Q. Tan, G. Wu, Atomically dispersed Fe-Co dual metal sites as bifunctional oxygen electrocatalysts for rechargeable and flexible Zn-air batteries, ACS Catal. 12 (2022) 1216–1227, https://doi.org/10.1021/acscatal.1c04550.